

Cite this: *Nanoscale*, 2012, **4**, 1190

www.rsc.org/nanoscale

PAPER

High-precision imaging of an encapsulated Lindqvist ion and correlation of its structure and symmetry with quantum chemical calculations^{†‡}

Elena Bichoutskaia,^a Zheng Liu,^b Navaratnarajah Kuganathan,^a Eric Faulques,^{ac} Kazu Suenaga,^b Ian J. Shannon^d and Jeremy Sloan^{*e}

Received 30th October 2011, Accepted 20th December 2011

DOI: 10.1039/c2nr11621a

Low-voltage aberration-corrected transmission electron microscopy (AC-TEM) of discrete Lindqvist $[\text{W}_6\text{O}_{19}]^{2-}$ polyoxometalate ions inserted from an ethanolic solution of $[\text{NBu}_4]_2[\text{W}_6\text{O}_{19}]$ into double walled carbon nanotubes (DWNTs) allows a higher precision structural study to be performed than previously reported. W atom column separations within the constituent W_6 tungsten cage can now be visualized with sufficient clarity that reliable correlation with structural predictions from density functional theory (DFT) can be achieved. Calculations performed on $[\text{W}_6\text{O}_{19}]^{2-}$ anions encapsulated in carbon nanotubes show good agreement with measured separations between pairs of W_2 atom columns imaged within equatorial WO_6 polyhedral pairs and also single W atom positions located within individual axial WO_6 octahedra. Structural data from the tilted chiral encapsulating DWNT were also determined simultaneously with the anion structural measurements, allowing the influence of the conformation of the encapsulating tubule to be included in the DFT calculation and compared against that of other candidate encapsulating nanotubes. Additional DFT calculations performed using Li^+ cations as a model for the $[\text{NBu}_4]^+$ counterions indicate that the latter may help to induce charge transfer between the DWNT and the $[\text{W}_6\text{O}_{19}]^{2-}$ ion and this may help to constrain the motion of the ion *in situ*.

1 Introduction

In tandem with the burgeoning interest in a wide diversity of nanoscale structures, associated studies into single molecules are becoming ever more prevalent. Advances in atomic probe-type (*i.e.* AFM, STM or similar)^{1–5} and electron microscopy^{6–8} atomic and molecular imaging techniques are making the efficient comparison between experimentally determined discrete structures and theoretical predictions more routine, permitting

a deeper understanding of structural fluctuations and interactions on a species-by-species basis. A key aspect of these investigations is the correlation of intra-molecular perturbations with effects induced by the local environment. These will depend on how the species is situated, for example, whether it is rendered into the gas phase, mounted on an atomically flat surface or inserted into a porous medium. Similarly, we must also take into account whether the molecule is in a charged or neutral state as this will affect how it interacts with the local environment,

^aSchool of Chemistry, University of Nottingham, University Park, Nottingham, NG7 2RD, UK

^bNanotube Research Center, National Institute of Advanced Industrial Science and Technology (AIST), Higashi 1-1-1, Tsukuba, 305-8565, Japan

^cInstitut des Matériaux Jean Rouxel, CNRS, UMR6502, Université de Nantes, 2 rue de la Houssinière, 44322 Nantes, France

^dDepartment of Chemistry, University of Birmingham, Edgbaston, Birmingham, B15 2TT, UK

^eDepartment of Physics, University of Warwick, Coventry, Warwickshire, CV4 7AL, UK. E-mail: j.sloan@warwick.ac.uk; Fax: +44 (0)2476692016; Tel: +44 (0) 24765 23392

[†] The DWNTs used in this experiment were supplied by the company CNI (Carbon Nanotechnology Inc.), now Unidym. A new sample of $[\text{nBu}_4\text{N}]_2[\text{W}_6\text{O}_{19}]$ was prepared according to a published procedure²⁷ and then inserted into DWNTs from an ethanolic solution using the procedure described in ref. 16. The 300 kV HR-TEM image of the $[\text{nBu}_4\text{N}]_2[\text{W}_6\text{O}_{19}]$ @DWNT composite was previously obtained on

a JEOL 3000F instrument with an objective C_s of 0.6 mm and an accelerating voltage of 300 kV. 80 kV images were obtained from the freshly prepared $[\text{nBu}_4\text{N}]_2[\text{W}_6\text{O}_{19}]$ @DWNT composite in a JEOL 2010F AC-TEM equipped with a CEOS aberration corrector for which C_s was tuned to 0.001 mm. All image simulations were performed using the multislice package SimulaTEM.⁴² Additional measurements were performed with the commercially available Gatan Digital Micrograph software and structure models were assembled using CrystalMaker software and standard Shannon anion and cation radii. Nanotube models were generated using the program Nanotube Modeler from JCrystalSoft (©2004–2011). DFT calculations were performed using the CASTEP program⁴³ which made extensive use of the High Performance Computing (HPC) facility at the University of Nottingham.

[‡] Electronic supplementary information (ESI) available: Computational methods (CASTEP) and vibrational analysis; unit cell assignments for DFT calculations; and RMSD analysis description. See DOI: 10.1039/c2nr11621a

influence any dynamical behaviour and also tend to modify the local electronic structure of the host medium. Finally, we need to take into account the steric relationship between the guest species and the encapsulating volume provided by a porous host as this will influence the translational and rotational behaviour of the guest molecule.

In addition to a large number of scanning probe (*i.e.* STM or AFM and adaptations) discrete molecule studies in which these are mounted on atomically flat or chemically modified impervious substrates,^{9,10} recent work has shown that structural studies can also be conducted on single molecules inserted into porous materials such as carbon nanotubes which have facilitated imaging studies by high resolution transmission electron microscopy (HR-TEM).^{6–8} Recently, a compromise between local probe and HR-TEM imaging studies has been achieved in that electron transparent monolayer materials such as graphene,^{11,12} monolayer boron nitride¹³ and graphene oxide^{14,15} can be used to image supported macromolecular or molecular-scale species with surface-type structure interactions being observed as a result.¹⁵ These latter results correlate well with related structural studies of molecules mounted on flat substrates and, as such, provide important clues on how these species will behave in surface-specific applications such as catalysis or directed surface assembly. In this regard, studies on the specific orientational behaviour of polyoxometalate ions or within porous media are also valuable as these ions are faceted and their ionic character can be tuned so that the energetics of capillary interactions can be studied in detail. We have already observed that these types of anions exhibit preferred orientations within nanotube capillaries and constrained translational motion suggesting a “ratchet”-like motion behaviour.¹⁶

Structural studies of anions and other molecular scale species can be made more extensive by reducing the aberrations in the imaging electron microscope^{8,15} and, at the same time, subjecting the structural information thereby obtained to a more detailed and rigorous theoretical analysis. Ideally we should be able to obtain good quality structural information from the encapsulating nanotube as this can be either semiconducting or metallic according to its structural conformation^{17,18} which can potentially have an impact on or be modified by the encapsulated anions, affecting their electronic properties.

Polyoxometalate ions (POMs) are of significant interest and have an extensive structural-synthetic chemistry enabling them to be produced as ordered molecular-scale cluster anions. These ions are formed in solution by oligomerization processes from transition metal oxide polyhedra^{19–22} and POMs show significant potential in a wide range of applications varying from catalysis to information storage and can also act as building blocks to form elegant ordered mesoscale structures.²³ One of their more significant properties is their ability to form a wide range of ordered ions with variable charge ordering arrangements on a molecular scale²⁴ and variable electron configurations making them highly desirable as nanoscale spin-ordered devices²⁵ and as agents for producing assemblies with other mesoscale systems including dendrons.²⁶ In the present context, they provide a heavy atom template with a clearly defined structural motif that can be readily imaged by HR-TEM when the anions are mounted within carbon nanotubes¹⁶ or when deposited on graphene oxide.¹⁵

Tungsten-based polyoxometalate ions, including the $[\text{W}_6\text{O}_{19}]^{2-}$ Lindqvist ion (prepared as $[\text{nBu}_4\text{N}]_2[\text{W}_6\text{O}_{19}]^{2-}$)²⁷ and the $[\gamma\text{-SiW}_{10}\text{O}_{36}]^{8-}$ lacunary Keggin ion (prepared as $\text{K}_8[\text{SiW}_{10}\text{O}_{36}]$),¹⁵ have been imaged both within double walled carbon nanotubes (DWNTs)¹⁶ and on monolayer graphene oxide (GO)¹⁵ with atomic resolution. In the latter case, the discrete ions moved during image acquisition frequently to the extent that composite images made up of at least two projections were obtained. $[\text{W}_6\text{O}_{19}]^{2-}$ Lindqvist super-octahedra (Fig. 1(a)) with a nominal gas-phase symmetry O_h when mounted within DWNTs moved more slowly in the electron beam and it was possible to visualize their structure more clearly. Pairs of tungsten atom (*i.e.* W_2) columns within the equatorial plane of the anion and diffuse contrast from single tungsten (*i.e.* W) columns could be imaged whenever the ion was imaged along its two-fold C_2 axis (see Fig. 1(c)).

A significant benchmark in performing such studies will be producing structural data of sufficient quality that can be compared against structure refinements produced by first-principles quantum mechanical calculations. However, a limitation of the previous imaging study of $[\text{W}_6\text{O}_{19}]^{2-}$ anions in DWNTs¹⁶ was that information from the single W atom columns was blurred or missing. A minimum requirement for an effective comparison with theory is that at least two structural dimensions of the anion should be resolved as this will determine whether or not the anion retains an ideal O_h symmetry or whether it distorts into lower symmetry within the nanotube. We demonstrate that not only is it possible to obtain high quality structural information from individual $[\text{W}_6\text{O}_{19}]^{2-}$ anions that can be directly compared against theoretical predictions but also we are able to obtain conformational information from the nanotube that

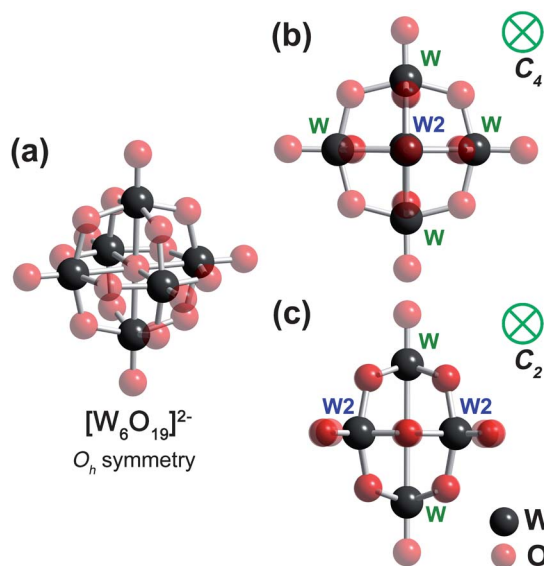


Fig. 1 (a) Perspective view of $[\text{W}_6\text{O}_{19}]^{2-}$ anion in an optimised O_h geometry. (b) View of the anion along C_4 with four single atom W columns and the axial W_2 atom pair indicated. (c) View of the anion along C_2 with the two equatorial W_2 atom pairs and two axial W single atom columns indicated. Note that, in this projection, the two peripheral O_3 columns in the equatorial plane are closer in proximity to the two W_2 columns than to the central O_3 column arranged along C_2 .

allows us to produce trial conformations of these for investigating both structural and electronic interactions between the encapsulated anion and the encapsulating nanotube.

2 Electron microscopy structural studies

2.1 80 kV aberration corrected imaging of $[\text{W}_6\text{O}_{19}]^{2-}$ @DWNT

The previous imaging study of $[\text{W}_6\text{O}_{19}]^{2-}$ anions mounted within DWNTs revealed that within sterically matched nanotubes (with an innermost SWNT having a diameter of ~ 1.2 nm) the ions lie with a preferred orientation within the encapsulating volume, specified by the van der Waals radii of the wall carbons (*i.e.* 0.17 nm) of *ca.* 0.9 nm.¹⁶ This orientation (which is projected along the C_2 axis of the anion—see Fig. 1(c)) conveniently enables W_2 – W_2 atom column pairs within the equatorial plane of the W_6O_{19} superoctahedron to be directly visualised by TEM. As the W cations are themselves fixed within the WO_6 suboctahedra, we need to take into account the contribution of oxygen and, if addressable, that of any counter-ions to the image contrast. In the previous work, the encapsulated anion was imaged at 300 kV in a conventional HR-TEM with an objective lens coefficient of spherical aberration (*i.e.* C_s (or, alternatively, C_3)) of 0.6 mm. Multislice image simulation studies showed that this level of aberration blurs the image contrast from the W_2 – W_2 atom column pairs once the contribution of the equatorial terminal oxygen atoms is taken into account. Furthermore we must be concerned about the possibility of extensive beam damage not only to the encapsulating carbon atoms, which have a threshold for knock on damage of 86 keV,^{28,29} but possibly also to the $[\text{W}_6\text{O}_{19}]^{2-}$ anion which may lose oxygen during high kinetic energy electron beam irradiation. Partial disintegration of the ion was observed when imaged at 300 kV, which was manifested in terms of a contraction in the measured W_2 – W_2 spacing over a period of 90 s from the initial exposure and extensive damage to the containing nanotube.¹⁶

In the present work we have completed a higher resolution aberration corrected TEM imaging (*i.e.* AC-TEM) study of the $[\text{W}_6\text{O}_{19}]^{2-}$ anions using a lower electron accelerating voltage of 80 kV, the enhanced resolution being provided (*i.e.* not withstanding the longer electron wavelength) by hardware spherical aberration correction using a much lower value of C_s (*i.e.* 0.001 mm as opposed to 0.6 mm in the previous study). The impact of these improved imaging conditions is evident in Fig. 2(a)–(c) and these improvements can be correlated with associated multislice image simulation studies (*i.e.* Fig. 2(d) and (e)). As in the previous study, we find that the $[\text{W}_6\text{O}_{19}]^{2-}$ anion locks into position with a preferred orientation in DWNTs for which the internal volume is matched sterically with the external volume of the anion.¹⁶ In terms of the relative orientation of the anion and also its imaging properties, we find that a large fraction of the anions align with the twofold C_2 axis aligned parallel to the electron beam such that two pairs of W atoms (*i.e.* the W_2 pairs indicated in Fig. 1(c)) situated within four WO_6 octahedra in the equatorial plane of the $[\text{W}_6\text{O}_{19}]^{2-}$ anion image as strong black spots within corresponding lattice images (*i.e.* Fig. 2(a)–(c)). Weaker spots correspond to single W atoms located within two single WO_6 octahedra situated above and below the equatorial plane of the anion (*i.e.* the W columns indicated in Fig. 1(c)).

Fig. 2(a) shows a wider field of view image of two parallel DWNTs, one empty and one containing a discrete $[\text{W}_6\text{O}_{19}]^{2-}$ anion, lying over some graphitic material towards the lower right of the main image. Comparison of the details of the same structure anion as imaged using the higher voltage (*i.e.* 300 kV) aberrated electron imaging system ($C_s = 0.6$ mm) in Fig. 2(b) with the same structure anion using the lower voltage (*i.e.* 80 kV) and reduced aberration ($C_s = 0.001$ mm) imaging conditions in Fig. 2(c) clearly shows the improvement in detail afforded by the latter. Not only are the dark spots corresponding to the W_2 columns more clearly visible in Fig. 2(c) but, additionally, significantly enhanced contrast from the single W atom columns is now observed.

A semi-quantitative indication of the improvement in precision between the aberrated and unaberrated HR-TEM images can be made using line profiles through W_2 – W_2 and W – W atom column pairs using multislice image simulations produced for both cases (*i.e.* Fig. 2(d) and (e)) as shown by the extracted equatorial and axial line profiles shown in Fig. 3(a) and (b), respectively. The simulations clearly show the greater precision that we anticipate for the experimental images, especially with regards to the measurement of the W_2 – W_2 atom column separations. As noted previously, there is an approximately 5% distortion in the W_2 – W_2 equatorial atom column separation relative to the positions anticipated from the bulk X-ray crystal structure. This was attributed in part to the high value for C_s but also to the smearing contribution of the two O_3 columns on the periphery of the anion along the equatorial plane (see Fig. 1(c)).¹⁶ This distortion is reproduced in the lower line profile I in Fig. 3(a) in which the two troughs of the profile corresponding to the W_2 columns are displaced by *ca.* 5% with respect to their expected positions (given by vertical black lines in Fig. 3(a)). Profile II in Fig. 3(a) corresponds to the simulated W_2 – W_2 atom column pairs for the AC-TEM with 80 kV accelerating voltage but also with a greatly reduced value for C_s (*i.e.* 0.001 mm). In this instance, the centres of the troughs corresponding to the W_2 columns are only displaced *ca.* 1% from the anticipated W_2 positions reflecting a much greater confidence in the new measurements (below) relative to the previous study.

According to the second set of line profiles III and IV (Fig. 2(b)), there is relatively little distortion of the axial W – W single atom columns in either the 300 kV or 80 kV images but, in the event, the HR-TEM image contrast from the experimental 300 kV image (*i.e.* Fig. 2(b)) is too noisy to reproduce a reliable line profile and measurement of this separation in the previous study was only roughly estimated. In Fig. 3(c) we see that it is possible to measure the atom column spacings for both the equatorial (line profile E) W_2 – W_2 atom column pair and the axial (line profile A) W – W atom column pair with reasonable precision. These new experimental measurements allow us to determine the W_2 – W_2 separation and the W – W separation as 0.342 nm and 0.477 nm, respectively, with an estimated precision of ± 0.026 nm which corresponds to the minimum pixel size of the unprocessed digital images which depends on the magnification in relation to the CCD pixel density and is not therefore a true measure of the resolution of the imaging microscope. Although this precision is apparently similar to that estimated in the 300 kV study,¹⁶ it is important to note that in the previous study, the

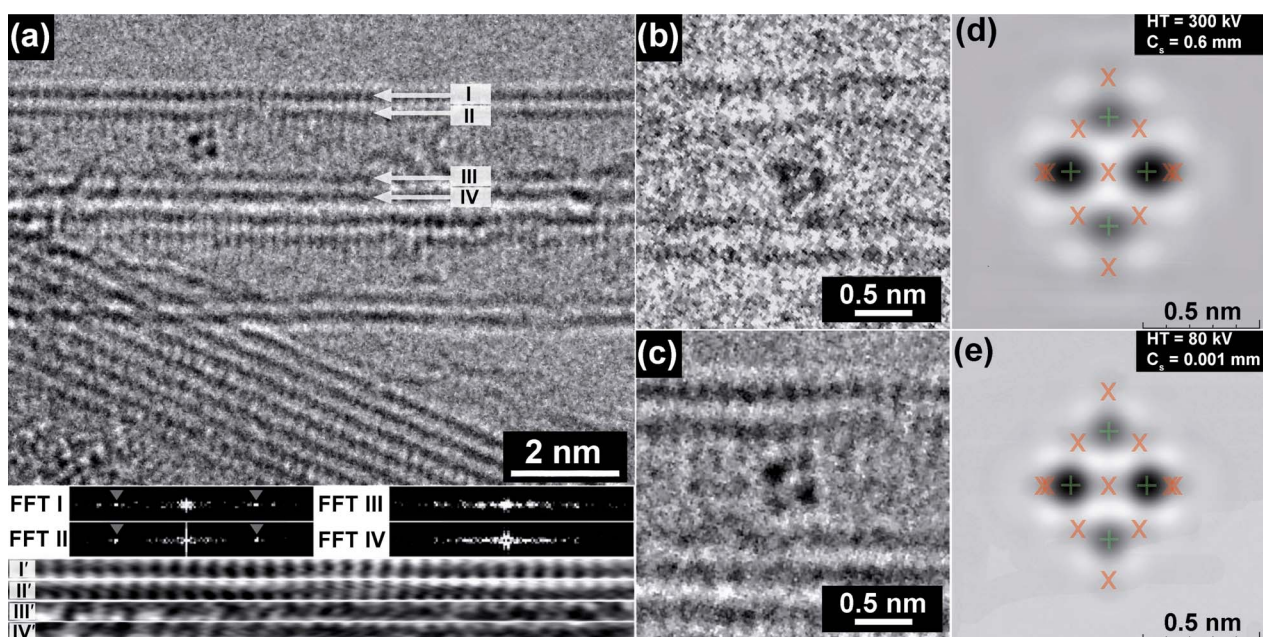


Fig. 2 (a) Field of view 80 kV AC-TEM image of a discrete $[\text{W}_6\text{O}_{19}]^{2-}$ anion imaged within one of a pair of DWNTs lying over (or under) some graphitic carbon material. Note that both DWNTs exhibit wall carbon spacing contrast on their respective uppermost walls but not on their lower walls indicating that the nanotubes are side by side as imaged and are not superimposed. The four indicated walls (*i.e.* I–IV) therefore belong to the uppermost encapsulating DWNT and not to the lower empty DWNT. Insets in the lower part of the image are four 1D fast Fourier transforms (FFTs) obtained from the real space image of the four indicated walls I–IV and below these are four inverse-FFT filtered images corresponding to the same respective regions (*i.e.* I'–IV'). (b) Detailed image of a discrete $[\text{W}_6\text{O}_{19}]^{2-}$ anion imaged at 300 kV from the previous study.¹⁶ (c) Details from (a) showing the improvement in detail at 80 kV but with C_3 tuned to 0.001 mm. (d) Multislice image simulation produced for the imaging conditions (inset) employed in (b). (e) Multislice image simulation produced for the imaging conditions (inset) employed in (a) and (c). In (d) and (e) the O atom positions are indicated by red crosses and the W atom positions are indicated by green “+” symbols.

observed W_2 – W_2 atom column separation is a convolution of the W_2 column contrast with that of the peripheral O_3 columns in projection (see Fig. 1(c)) following distortion by the imaging

system. The simulations in Fig. 3(a) indicate that the contrast contributed by W_2 atom columns is now predominantly due to W rather than O following hardware aberration correction.

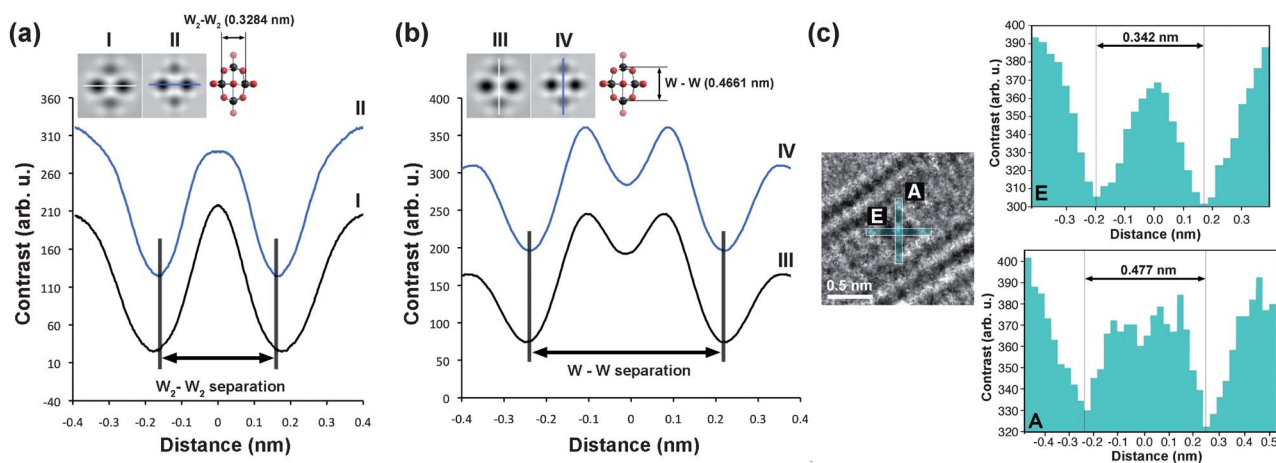


Fig. 3 (a) Pair of line profiles through the equatorial W_2 – W_2 columns in the $[\text{W}_6\text{O}_{19}]^{2-}$ anion obtained from the multislice simulations in Fig. 2(d) and (e) which are also shown as insets at the top left of the figure. I (black trace) denotes the contrast corresponding to the 300 kV, $C_3 = 0.6$ mm, II (black trace) denotes the contrast corresponding to the 80 kV, $C_3 = 0.001$ mm. The vertical black lines denote the actual physical W_2 – W_2 separation (*i.e.* 0.3284 nm) as depicted in the model at top right and determined for the bulk $[\text{W}_6\text{O}_{19}]^{2-}$ anion. (b) As for (a) but this time the line profiles are obtained through the axial W – W single atom columns, as depicted in the simulations and model at the top left of the figure. The vertical black lines indicate the actual separation between the W – W columns in the bulk structure (*i.e.* 0.4661 nm). (c) Detail from the experimental 80 kV AC-TEM image of the $[\text{W}_6\text{O}_{19}]^{2-}$ anion encapsulated within a DWNT (left). 5 pixel wide experimental line profiles through the dark spots corresponding to the W_2 – W_2 columns as indicated in detail on the left. Plot E (top) illustrates the line profile obtained through the equatorial W_2 – W_2 separation. Plot A (bottom) illustrates the line profile obtained through the axial W – W atom column pair.

2.2 Influence of the nanotube tilt on imaging and calculations

A further benefit of the higher resolution AC-TEM imaging of the $[\text{W}_6\text{O}_{19}]^{2-}$ @DWNT composite was the ability to resolve the wall carbon spacings of the encapsulating nanotube which was not achieved in the previous study due to either insufficient resolution or the encapsulating nanotube being in an unfavourable orientation or conformation.¹⁶ This consideration is important because of the well-known relationship between the nanotube wrapping (or 'roll-up') vector (C_h) and the electronic band structure of the obtained nanotube as a function of this which may influence our band structure calculations (see below).^{17,18} The ability to see such finely resolved detail in carbon nanotubes depends on the following factors with regards to the nanotube and also the imaging electron microscope: (i) the wrapping vector of the carbon nanotube (*i.e.* $C_h = n\mathbf{a}_1 + m\mathbf{a}_2$ where \mathbf{a}_1 and \mathbf{a}_2 are the basis vectors of the graphene sheet making up the nanotube and n and m are integers, (n, m) being the essential conformation of a given nanotube); (ii) the angle of tilt (ϕ) of the nanotube with respect to the electron beam; and (iii) the resolving power of the TEM used to image the nanotubes.^{30,31}

For zig-zag SWNTs (*i.e.* with $n = 1, 2, 3 \dots n, m = 0$), the wall carbon columns can be imaged by most high quality HR-TEM instruments with a resolution better than 0.2 nm. For SWNTs that approximate to an armchair configuration (*i.e.* $n = m$), the wall carbons are too close together to be imaged effectively in most uncorrected HR-TEMs. In the case of a chiral nanotube (*i.e.* $n \neq m > 0$), the wall carbon spacings can only be seen effectively if the nanotube is tilted by a particular value of ϕ with respect to the wrapping vector of the nanotube.^{30,31} The chiral tube will display resolvable contrast (*i.e.* depending on the resolving power of the HR-TEM) on one tube wall only if the value of the difference $\delta = |\alpha - \phi|$ is small where $\alpha = \angle(C_h, \mathbf{a}_1) = \arctan[\sqrt{3}m/(2n + m)]$ with α being the chiral angle.³⁰

In the experimental image in Fig. 2(a) (and also the in detail in Fig. 2(c)), we see that not only the anion but also the wall carbons of the encapsulating DWNT are clearly resolved but only on the top surface of the carbon nanotube. Furthermore, we observe that both the inner and outer SWNTs exhibit 0.21 nm wall carbon spacings (*i.e.* Fig. 4(a)) and that are in register with each other indicating that both SWNTs share a compatible wrapping vector in that both exhibit similar wall carbon spacings on one side only which is consistent with the observation that DWNTs frequently form with commensurate interlayer stacking on at least one surface even if the chiral angles are not completely aligned.³² This clearly indicates that both SWNTs comprising the nanotube are chiral (*i.e.* neither armchair or zigzag) and, additionally, the entire composite must be tilted by some angle ϕ with respect to the electron beam. In exhaustively examining all of the conformational possibilities for the encapsulating nanotube (taking into account the diameters of both the inner and outer SWNTs), a relatively small number of candidates emerge and for the purpose of the current work, a good compatible DWNT candidate is the chiral pair (12,6)@(18,9). How we can eliminate other potential DWNT candidates will be discussed more fully in a subsequent publication (in preparation).

For the chosen (12,6)@(18,9) DWNT candidate, we can verify the relationship between the angle of tilt (ϕ) by performing

multislice image simulations on tilted *versus* untilted nanotubes (*i.e.* Fig. 4(b) and (c)). Untilted chiral DWNTs do not produce observable wall carbon spacings on either of the opposing walls of the DWNT (*i.e.* top model, Fig. 4(b) and Fig. 4(c), top simulation). On the other hand, tilting the nanotube by a small angle (*e.g.* $\phi = 12^\circ$) as indicated in Fig. 4(b) (bottom model) produces a clearly discernible wall carbon spacing in both SWNTs comprising the DWNT on the top surface in the image simulation (*i.e.* Fig. 4(c), bottom). Tilting the composite in the opposite sense to that depicted in Fig. 4(b) produces complementary wall carbon spacings on the opposing walls of the constituent SWNTs. Inspection of the (12,6)@(18,9) DWNT composite from a perspective end-on view (Fig. 4(d)) shows that the nanotubes are a good match in terms of their respective wrapping vectors and this produces the 'in register' behaviour of the commensurate SWNT pair.

2.3 Dynamical motion of $[\text{W}_6\text{O}_{19}]^{2-}$ anions within DWNTs and viewing the $[\text{W}_6\text{O}_{19}]^{2-}$ anion along C_4 axis

In DWNTs with an internal diameter (as specified by the innermost SWNT, see above) slightly higher than 1.2 nm, we found that the $[\text{W}_6\text{O}_{19}]^{2-}$ anions both rotate and translate discontinuously within the capillaries so that it was possible to visualise the anion along different symmetry axes. Previously this was achieved only by simulating the anion along various projections by rotating the anion systematically about two orthogonal axes through the centre of gravity of the anion.¹⁶ In the present work we are able to see more dynamical rotational behaviour by recording sequences of time-resolved 0.8 s exposures (in addition to a 1.0 s minimum refresh time for the CCD) obtained at a single defocus over timescales of up to a minute in the AC-TEM. In general we found that the anions did not significantly distort, as reported in the 300 kV imaging study and, additionally, we did not observe significant damage to the encapsulating DWNTs during image acquisition over the stated time periods. In some nanotubes, we observed significant motion of the encapsulated anions and this could take the form of either *in situ* translation or rotation.

In Fig. 5(a), we see an extended time resolved series of images in which two well separated $[\text{W}_6\text{O}_{19}]^{2-}$ anions can clearly be discerned but only one of them is visible for the entire series. The first anion (demarcated by a series of yellow boxes) is visible in the first image and in all the subsequent images. This anion only moves slightly under the influence of electron bombardment but is seen to rotate *in situ*. Several clearly defined orientations of the anion are observed as indicated by the labels i–v. Intriguingly, the anion is imaged for the first time in the AC-TEM along the four-fold C_4 axis (*cf.* Fig. 1(b)) at ii and iii after 4.4 s and 9.8 s total elapsed time, respectively. This anion undergoes further rotation *in situ* but eventually rotates to the more commonly observed C_2 projection at v and after 27.8 s total elapsed time. These projections are verified with additional image simulations in Fig. 5(b) (*i.e.* top model and simulation and middle model and simulation).

After 15.2 s of total elapsed time, we see a second $[\text{W}_6\text{O}_{19}]^{2-}$ anion appearing from the left of the field of view and this is demarcated in this and the four subsequent images by red boxes. This anion exhibits reasonably well-defined orientations at vi and

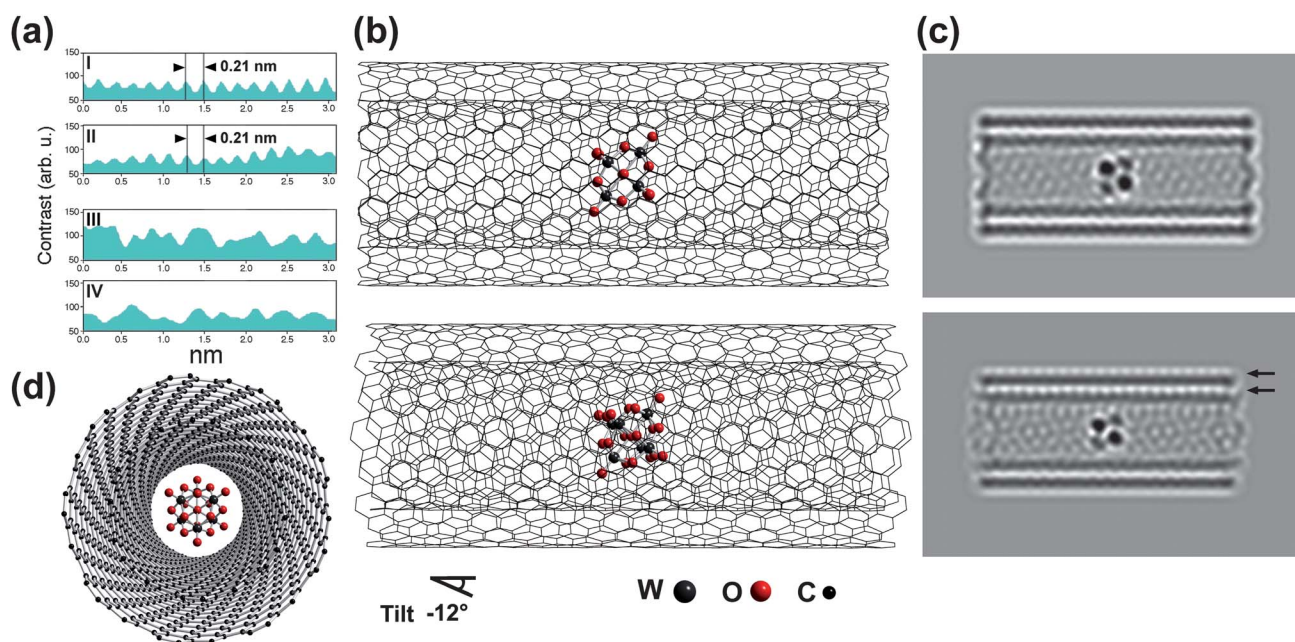


Fig. 4 (a) Line profiles I–IV obtained through the four filtered line profiles I'–IV' in the bottom part of Fig. 2(a). I' and II' correspond to the uppermost SWNT walls whereas III' and IV' correspond to the two lower SWNT walls of the DWNT. The upper two walls have a periodicity of *ca.* 0.21 nm whereas the lower walls are aperiodic. (b) Two structure models corresponding to a [W₆O₁₉]²⁻ anion mounted within a (12,6)@(18,9) DWNT nanotube. The top model is untitled and the bottom model is tilted 12° out of the plane of the page, as indicated. (c) Multislice image simulations produced from the two configurations in Fig. 4(b). Note that only the bottom simulation corresponding to the tilted DWNT exhibits wall carbon spacings on the uppermost two walls. (d) Perspective end-on model of the [W₆O₁₉]²⁻@(12,6)@(18,9) DWNT in Fig. 2(b). In this projection, it is easy to see that the two nanotubes are matched in terms of their respective wrapping vectors.

vii. The latter corresponds again to the common C_2 projection and this is verified with the model and image simulation in Fig. 5(b).

The diameter of the innermost SWNT of the DWNT imaged in Fig. 5(a) is *ca.* 1.2 nm, consistent with that of the previous study and also the other imaged nanotube in Fig. 2(a). Also, we

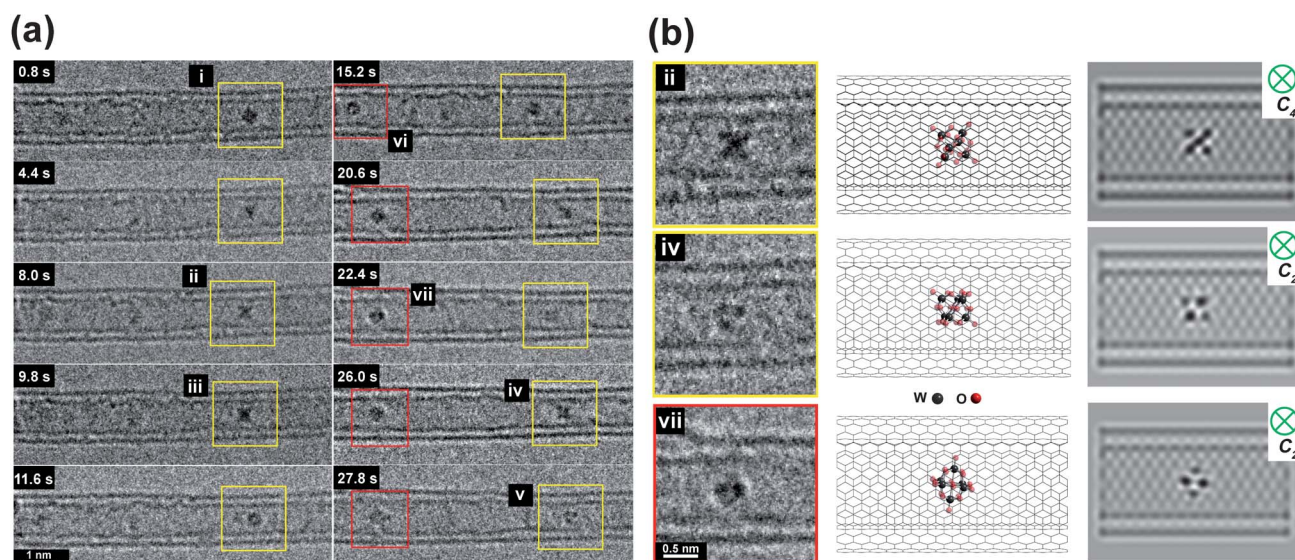


Fig. 5 (a) Time-resolved sequence of AC-TEM image of dynamical rotation/translation of two [W₆O₁₉]²⁻ anions within a 1.2 nm internal diameter DWNT. In the first five images (*i.e.* up to 11.6 s elapsed time), only one anion is clearly visible (yellow boxes) which rotates during the conditions of the image acquisition. A second anion appears in the field of view after 15.2 s and this also rotates *in situ* towards the end of the sequence (red boxes). For the first ion, clearly defined orientations are visible at positions i–v. For the second ion clearly defined orientations are visible at positions vi and vii. (b) Details, corresponding models and multislice simulations for positions ii, iv and vii. Note that the first anion is imaged first along C₄ (*i.e.* position ii) and then rotates inside the DWNT so that it is also imaged along C₂. At position vii the second anion is imaged along C₂. In iv and vii the anion is blurred due to motion during the 0.8 s exposure.

note that the wall carbon contrast of this nanotube is not resolved on either the upper or lower wall pairs which indicates that the conformation of both the inner and outer SWNTs comprising the nanotube is close to armchair.

3 Quantum chemistry calculations

3.1 Impact of local environment on the anion structure

In order to study the effect of confinement, the $[\text{W}_6\text{O}_{19}]^{2-}$ anion was optimized in five different environments including two gas phase conditions, periodic and non-periodic, and inside three carbon nanotubes of different chiralities (see the Computational methods section in the ESI†). The optimized geometry of the $[\text{W}_6\text{O}_{19}]^{2-}$ anion in the gas phase was obtained both with and without symmetry constraints, and it showed no significant distortion from the expected octahedral symmetry. This result is in agreement with previous calculations^{33–35} and experiments,³⁶ obtained as O_h symmetry averages on bond length values observed in crystalline phases. The octahedral symmetry of the $[\text{W}_6\text{O}_{19}]^{2-}$ anion has been also confirmed by the vibrational analysis presented in the ESI†.

The (12,6), (16,0) and (9,9) SWNTs were selected to match the diameter of the inner wall of a DWNT identified in the experiment (Fig. 4). The structures of the (12,6), (16,0) and (9,9) SWNTs were initially optimized without the presence of the ion, yielding diameters of 1.243 nm, 1.253 nm and 1.220 nm, respectively. The subsequent structure optimization of the $[\text{W}_6\text{O}_{19}]^{2-}$ anion inside these nanotubes was produced allowing full relaxation of both the ion and the nanotube wall in periodic boundary conditions. Two unit cells of a (12,6) SWNT, four unit cells of a (16,0) SWNT, and eight unit cells of a (9,9) SWNT were used to encapsulate one Lindqvist ion, thus maximizing the distance between the ion and its image along the nanotube principal direction. The ion–ion separation along the nanotube axis was therefore set to be 2.25 nm in a (12,6) SWNT, 1.70 nm in a (16,0) SWNT and 1.97 nm in a (9,9) SWNT. These arrangements are depicted schematically in Fig. S1 (ESI†). In order to check that periodic images of the ion did not adversely affect the results, the structure of the ion was optimized using the same periodic boundary conditions as for a (9,9) SWNT, but without the presence of the nanotube. Within the accuracy of the calculations it was found to be the same as the structure of the ion in the gas phase.

Our calculations show that if the $[\text{W}_6\text{O}_{19}]^{2-}$ anion retains its negative charge (–2) inside the nanotube it does not bind to the nanotube and the overall structure is unstable (see Section 3.3, Interaction between the anion and carbon nanotube). In the present AC-TEM investigation of the $[\text{W}_6\text{O}_{19}]^{2-}$ anion inside a DWNT, we have still not been able to account for the location of the counterbalancing $[\text{NBu}_4]^+$ counter-ions. In our calculations, however, the presence of counter-ions in a nanotube has been shown to (i) affect the stabilisation of the interacting system and (ii) lower the anion symmetry. To identify possible changes in the symmetry of the encapsulated anion, two types of the geometry optimization calculations were produced using three selected SWNTs. In the first geometry optimization, two additional free Li^+ ions were added to the (now neutral) supercell containing the $[\text{W}_6\text{O}_{19}]^{2-}$ anion inside a SWNT. The Li^+ ions

were located at fractional coordinates (1/4) and (3/4) along the SWNT axis, and the anion was placed in the middle. In this case, the Li^+ ions orient themselves towards the octahedral faces of the encapsulated $[\text{W}_6\text{O}_{19}]^{2-}$ anion and shift off their original position in the cell towards the octahedral faces. In the second geometry optimization containing counter-ions, the two Li^+ ions were placed in the position relative to the ion in the bulk crystalline phase of $[\text{NBu}_4]_2[\text{W}_6\text{O}_{19}]$ as determined by single crystal X-ray diffraction.²⁷ In this case, the $[\text{W}_6\text{O}_{19}]^{2-}$ anion undergoes some structural distortion, mainly affecting the tungsten-bridge oxygen separations. In all of the nanotubes, the $[\text{W}_6\text{O}_{19}]^{2-}$ anion orientates itself in such a way that the average distance between the outer oxygen atoms and nanotube is maximized. This leads to a ‘tripod-down’ type orientation, where the octahedron formed by the oxygens has a face pointing in either direction along the tube and the other six faces are pointing at the tube walls.

Results comparing the structure of the $[\text{W}_6\text{O}_{19}]^{2-}$ anion in the gas phase and inside the SWNT environment are presented in Table 1. The gas phase geometry of the $[\text{W}_6\text{O}_{19}]^{2-}$ anion presented in the first numerical column is in a good agreement with previous theoretical values of $d_1(\text{W}-\text{O}_c) = 0.234$ nm, $d_2(\text{W}-\text{O}_b) = 0.194$ nm and $d_3(\text{W}-\text{O}_t) = 0.173$ nm.³³ The data presented in the second numerical column of Table 1 show no perturbation of the strong tungsten cage of the $[\text{W}_6\text{O}_{19}]^{2-}$ anion inside SWNTs. A root mean square deviation (RMSD) analysis of the resulting ion structures in the gas phase and inside SWNTs was performed using Kabsch algorithm.³⁷ The RMSD errors, which vary between 0.001 nm and 0.004 nm, are a further indication that the ion remains largely unperturbed when placed inside a SWNT. The calculated values of the W_2-W_2 and $\text{W}-\text{W}$ distances appear to fall within the estimated error of ± 26 pm for the experimental values of 0.342 nm and 0.477 nm, respectively, presented in this paper. The RMSD analysis is defined in the ESI†.

3.2 Effect of anion on the electronic structure of the nanotube

The density of states (DOS) has been calculated for the empty (12,6), (16,0) and (9,9) SWNTs and for the $[\text{W}_6\text{O}_{19}]^{2-}@\text{(SWNT)}$ systems. In all cases, the calculated DOS plots show very small modifications to the electronic structure of the host nanotubes although in all cases there is a charge transfer of approximately one electron from the anion to the host nanotube. As an example,

Table 1 The calculated geometry of the $[\text{W}_6\text{O}_{19}]^{2-}$ anion in the gas phase and inside a SWNT. At bottom, the experimentally determined W_2-W_2 and $\text{W}-\text{W}$ separations are indicated (all distances are given in nm)

Distances within $[\text{W}_6\text{O}_{19}]^{2-}$	$[\text{W}_6\text{O}_{19}]^{2-}$ environment	
	Gas phase	Inside SWNT or DWNT
W_2-W_2	0.333	0.330
$\text{W}-\text{W}$	0.471	0.470
O_t-O_t	0.816	0.812
$d_1(\text{W}-\text{O}_c)$	0.235	0.234
$d_2(\text{W}-\text{O}_b)$	0.194	0.193
$d_3(\text{W}-\text{O}_t)$	0.173	0.172
W_2-W_2 (exp)	—	0.342 ± 0.026
$\text{W}-\text{W}$ (exp)	—	0.477 ± 0.026

Fig. 6 presents the calculated DOS for an empty (12,6) SWNT and the $[\text{W}_6\text{O}_{19}]^{2-}@(\text{12,6})$ system. As expected a chiral (12,6) SWNT is shown to be metallic. The (12,6) SWNT remains metallic after encapsulation of the $[\text{W}_6\text{O}_{19}]^{2-}$ ion. The total DOS (red line) of the whole system is practically the sum of the partial DOS of the nanotube and the $[\text{W}_6\text{O}_{19}]^{2-}$ ion. The difference between the DOS of an empty (12,6) SWNT and that filled with the ion is very small at the Fermi level thus indicating a very weak interaction between a (12,6) SWNT and the ion (in this case, counter-ions were not present in the nanotube and dispersion interactions were not taken into account). It is quite typical for a SWNT to have the unchanged DOS at the Fermi level upon encapsulation. For example, recent DFT calculations³⁸ performed on the HgTe@SWNT system showed the same tendency, and it has been concluded that the DOS remains the same due to the minimal charge transfer and non-covalent nature of binding.

The tilt analysis in Section 2.2 gives us a way of discarding one possibility in favour of another and therefore the (16,0) and (9,9) SWNTs may be discarded for comparison with the experimental case (but may be valid for another experimental example *e.g.* Fig. 5). More accurate resolution of the conformation of the encapsulating DWNT may give a more definitive solution with respect to the nanotube conformation, particularly with regards to the inner SWNT which may not be in perfect register with the outer SWNT³² (*i.e.* as expressed in the idealized model in Fig. 4(d)) therefore allowing for a further refinement of this approach and a more rigorous solution that may later be compared against experimental physical measurements of localised DWNT or SWNT band gap modifications caused by ion inclusion.

3.3 Interaction between the anion and the nanotube

Without taking into consideration the presence of counter-ions, the system of the Lindqvist ion encapsulated within SWNT remains unstable. The stable configuration and the binding between the ion and SWNT have been found only when the system had no overall charge (neutral). In HRTEM images presented in this work, the contrast of single $[\text{nBu}_4\text{N}]_2[\text{W}_6\text{O}_{19}]$ molecules is still dominated by the six strongly scattering tungsten atoms. Individual $[\text{nBu}_4\text{N}]^+$ species give rise to

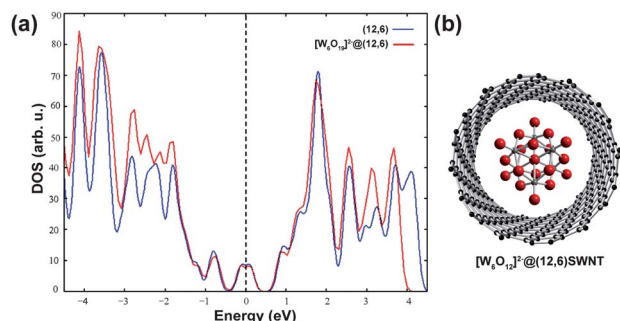


Fig. 6 (a) Density of states plot for the $[\text{W}_6\text{O}_{19}]^{2-}@(\text{12,6})$ SWNT. The blue line corresponds to the unfilled (12,6) SWNT and the red line to the (12,6) SWNT encapsulating the $[\text{W}_6\text{O}_{19}]^{2-}$ ion. The zero dotted line corresponds to the Fermi level. (b) Perspective structural depiction of the $[\text{W}_6\text{O}_{19}]^{2-}@(\text{12,6})$ SWNT system.

Table 2 The DFT binding energies for the $[\text{W}_6\text{O}_{19}]^{2-}@(\text{9,9})$ system in the absence and presence of counter-ions or a monovacancy on the nanotube wall

System	DFT binding energy/eV
$[\text{W}_6\text{O}_{19}]^{2-}@(\text{9,9})$	No binding
$[\text{W}_6\text{O}_{19}]^{2-}@(\text{9,9})$ with a monovacancy	No binding
$[\text{W}_6\text{O}_{19}]^{2-} + 2\text{Li}^+@(\text{9,9})$	-0.61

comparatively diffuse contrast due to the low atomic numbers of nitrogen and hydrogen. Although during imaging experiments we have not considered directly the effects of the $[\text{nBu}_4\text{N}]^+$ counter-ions, their presence in close proximity to the anion in order to maintain the stability and charge neutrality of the system became apparent from our theoretical modelling. Table 2 summarizes the calculated results obtained for the binding energies of the $[\text{W}_6\text{O}_{19}]^{2-}@(\text{SWNT})$ system in the absence and presence of counter-ions and a monovacancy on the nanotube wall. Although all three selected SWNTs show a similar interaction with the Lindqvist ion, a (9,9) SWNT has been used as an example as it has a smaller simulation cell than that of a (12,6) SWNT. It was found that DFT predicts binding only in the presence of two Li^+ counter-ions in SWNT. The interaction potential as a function of the ion displacement within a (9,9) SWNT is very flat, and the barrier to the relative motion of the ion along the nanotube axis is calculated to be less than 0.05 eV. This indicates that the ion is free to move inside SWNT, and that the barrier can be easily overcome at room temperature. The presence of a single monovacancy on the nanotube wall does not increase the binding of the ion to the wall and the barrier to the relative motion of the ion inside the nanotube remains very low. It must also be remarked here that even under 80 kV imaging conditions, some wall carbon defects are expected³⁹ but the rate of defect formation is very greatly reduced in comparison to the previously employed 300 kV imaging conditions.¹⁶

4 Concluding remarks and prospects

We have completed a new and higher resolution imaging study of discrete $[\text{W}_6\text{O}_{19}]^{2-}$ Lindqvist ions inserted into DWNTs and have succeeded in gaining significantly more detail with regards to their structure *in situ* and also that of the encapsulating nanotube. In particular, we are able to accurately obtain $\text{W}_2\text{-W}_2$ and W-W distance measurements from atom column imaging, allowing two key dimensions of the anion to be determined and compared against theoretical predictions with good agreement. Furthermore, it was possible to obtain conformational information from the encapsulating DWNT therefore allowing predictions concerning the local DOS of the composite material and structural optimisation of the included anion to be realised for the first time and compared against a real composite. Perhaps the most significant aspect of this study is that we have managed to demonstrate an effectively higher resolution study of the $[\text{W}_6\text{O}_{19}]^{2-}$ ion inside DWNTs in effect by reducing the convolution between the features of interest (*i.e.* the $\text{W}_2\text{-W}_2$ and W-W atom column separations) and other features in the anion and have greatly reduced both the inherent noise in the images and

the incipient beam damage to the anion. The obtained results are therefore much more readily comparable against theoretical calculations than the structural information obtained from the previously recorded images.¹⁶

One consideration in comparing the theoretically determined $[\text{W}_6\text{O}_{19}]^{2-}$ anion structures is whether or not the symmetry of the anion reduces from O_h to D_{4h} in terms of the rigidity of the W_6 cage. A simple way of doing this is to assume that the four W atoms in the equatorial plane lie on a perfect square, one side of which corresponds to the determined $\text{W}_2\text{--W}_2$ atom column separation. The W–W separation (*i.e.* $d_{\text{W--W}}$ in nm) in the equatorial plane will then correspond to the hypotenuse and this will correspond to $d_{\text{W}_2\text{--W}_2}/\cos 45^\circ$. If the anion has perfect O_h symmetry, then $d_{\text{W--W}}$ in the equatorial plane should be equivalent to $d_{\text{W--W}}$ in the axial plane and, indeed, for all of the determined values in Table 1, this is the case. With regards to the experimentally determined $d_{\text{W}_2\text{--W}_2}$ value, $d_{\text{W}_2\text{--W}_2}/\cos 45^\circ$ gives 0.483 nm rather than the experimentally determined value of 0.477 nm. However, this value does not deviate from the predicted value by more than the estimated error (*i.e.* ± 0.026 nm) and we cannot assume a lowering of symmetry on this basis alone. Theory predicts, however, that this deviation is reflected in the flexibility of the W–O bonds and not any flexibility of the W_6 cage and even our experimental results reflect this within the determined error.

The Lindqvist ion represents one of the smallest 3D objects studied by HR-TEM¹⁶ and now by AC-TEM. We anticipate that very many useful studies can be performed on related polyoxometalate and other molecular scale species that can be rendered more interesting by introducing a higher element of chemical tuning (for example, by mixing the number and type of atoms in the encapsulated anions) or by raising the charge on the included molecule although there remains significant work to be done even in the present context. We are still lacking useful information with regards to the $[\text{NBu}_4]^+$ counter-ions (*i.e.* in $[\text{NBu}_4][\text{W}_6\text{O}_{19}]$), although our DFT analysis provides the first tantalising evidence that these ions may play a role in terms of halting the transport and then stabilising the preferred orientation of the Lindqvist ion *in situ*, a result with possibly significant consequences for studies into the diffusion of non-neutral species along the normally “flat” potential energy surface (PES)⁴⁰ of nanotubes which normally smooth the transport of various species through them.⁴¹ Additionally, one would ideally like to have more information about the oxygen atoms in the $[\text{W}_6\text{O}_{19}]^{2-}$ anion as our calculations predict that it is predominantly the W–O bonds that cause the lowering in symmetry of the ion rather than the positioning of the W atoms themselves. The new higher resolution study indicates that the W_6 cage is not significantly distorted beyond O_h symmetry, a result that was difficult to predict from the previous lower resolution imaging study due to the absence of reliable information from the W–W single atom column separation (*i.e.* Fig. 3(b) and (c)).¹⁶ Although the results we have obtained thus far may not be seen as particularly surprising, on the other hand, we feel that we have significantly increased the confidence with which measurements can be made on such small-scale systems using the approaches described in the current work. When the results obtained reveal more spectacular conclusions, then we may view them with an even higher degree of confidence than hitherto.

Acknowledgements

J.S. is indebted to the Warwick Centre for Analytical Science (EPSRC funded grant EP/F034210/1) and to the AIST for additional financial support. Z.L. and K.S. acknowledge support from JST-CREST and also the Grant-in-aid from MEXT (19054017). Some of the equipment used in the preliminary characterization of $[\text{nBu}_4\text{N}]_2[\text{W}_6\text{O}_{19}]$ was obtained through the Birmingham Science City project “Creating and Characterising Next Generation Advanced Materials (AM1),” with support from Advantage West Midlands (AWM) and part funded by the European Regional Development Fund (ERDF). EB gratefully acknowledges financial support from an EPSRC-GB Career Acceleration Fellowship (EP/G005060).

Notes and references

- 1 D. M. Eigler and E. K. Schweitzer, *Nature*, 1990, **344**, 524.
- 2 F. Moresco, G. Meyer, K.-H. Reider, H. Tang, A. Gourdon and C. Joachim, *Phys. Rev. Lett.*, 2001, **87**, 088302.
- 3 L. Gross, *Nat. Chem.*, 2011, **3**, 273.
- 4 R. Temirov, S. Soubatch, O. Neucheva, A. Lassise and F. Tautz, *New J. Phys.*, 2008, **10**, 053012.
- 5 S.-W. Hla, *J. Vac. Sci. Technol., B: Microelectron. Nanometer Struct.–Process., Meas., Phenom.*, 2005, **23**, 1351.
- 6 B. W. Smith, M. Monthieux and D. E. Luzzi, *Nature*, 1998, **396**, 323.
- 7 Y. Sato, K. Suenaga, S. Okubo, T. Okazaki and S. Iijima, *Nano Lett.*, 2007, **7**, 3704.
- 8 Z. Liu, M. Koshino, K. Suenaga, A. Mrzel and H. Kataura, *Phys. Rev. Lett.*, 2006, **96**, 088304.
- 9 L. Gross, F. Mohn, N. Moll, P. Liljeroth and G. Meyer, *Science*, 2009, **325**, 1110.
- 10 L. A. Bottomley, J. N. Haseltine, D. P. Allison, R. J. Warmack, T. Thundat, R. A. Sachleben, G. M. Brown, R. P. Woychik, K. Jacobson and T. Bruce Ferrell, *J. Vac. Sci. Technol., A*, 1992, **10**, 591.
- 11 S. Iijima, *Micron*, 1977, **8**, 41.
- 12 J. C. Meyer, C. O. Girit, M. F. Crommie and A. Zettl, *Nature*, 2008, **454**, 319.
- 13 J. C. Meyer, A. Chuvilin, G. Algara-Siller, J. Biskupek and U. Kaiser, *Nano Lett.*, 2009, **9**, 2683.
- 14 N. R. Wilson, P. A. Pandey, R. Beanland, R. J. Young, I. A. Kinloch, L. Gong, Z. Liu, K. Suenaga, J. P. Rourke, S. J. York and J. Sloan, *ACS Nano*, 2009, **3**, 2547.
- 15 J. Sloan, Z. Liu, K. Suenaga, N. R. Wilson, P. Pandey, L. M. Perkins, J. P. Rourke and I. J. Shannon, *Nano Lett.*, 2010, **10**, 4600.
- 16 J. Sloan, G. Matthewman, C. Dyer-Smith, A.-Y. Sung, Z. Liu, K. Suenaga, A. I. Kirkland and E. Flahaut, *ACS Nano*, 2008, **2**, 966.
- 17 R. Saito, M. Fujita and M. S. Dresselhaus, *Phys. Rev. B: Condens. Matter Mater. Phys.*, 1992, **46**, 1804.
- 18 N. Hamada, S.-I. Sawada and A. Oshiyama, *Phys. Rev. Lett.*, 1992, **68**, 1579.
- 19 M. T. Pope and A. Müller, *Angew. Chem., Int. Ed.*, 1991, **30**, 34.
- 20 C. L. Hill and C. M. Prosser-McCartha, *Coord. Chem. Rev.*, 1995, **143**, 407.
- 21 J. T. Rhule, C. L. Hill, D. A. Judd and R. F. Schinazi, *Chem. Rev.*, 1998, **98**, 327.
- 22 W. Klemperer and C. Wall, *Chem. Rev.*, 1998, **98**, 297.
- 23 H. N. Miras, G. J. T. Cooper, D.-L. Long, H. Boegge, A. Müller, C. Streb and L. Cronin, *Science*, 2010, **327**, 72.
- 24 D. L. Long, E. Burkholder and L. Cronin, *Chem. Soc. Rev.*, 2007, **36**, 105.
- 25 J. Lehmann, A. Gaita-Arino, E. Coronado and D. Loss, *Nat. Nanotechnol.*, 2007, **5**, 312.
- 26 D. Volkmer, B. Breidenkötter, J. Tellenbröker, P. Kögerler, D. G. Kurth, P. Lehmann, H. Schnablegger, D. Schwahn, M. Pipenbrink and B. Krebs, *J. Am. Chem. Soc.*, 2002, **124**, 10489.
- 27 J. Fuchs, W. Freiwald and H. Hartle, *Acta Crystallogr., Sect. B: Struct. Crystallogr. Cryst. Chem.*, 1978, **34**, 1764.
- 28 F. Banhart, *Rep. Prog. Phys.*, 1999, **62**, 1181.
- 29 B. W. Smith and D. E. Luzzi, *J. Appl. Phys.*, 2001, **90**, 3509.

-
- 30 S. Friedrichs, J. Sloan, J. L. Hutchison, M. L. H. Green, R. R. Meyer and A. I. Kirkland, *Phys. Rev. B: Condens. Matter Mater. Phys.*, 2001, **64**, 045406.
- 31 Z. Liu, K. Suenaga, H. Yoshida, T. Sugai, H. Shinohara and S. Iijima, *Phys. Rev. Lett.*, 2005, **95**, 187406.
- 32 A. Hashimoto, K. Suenaga, K. Urita, T. Shimada, T. Sugai, S. Bandow, H. Shinohara and S. Iijima, *Phys. Rev. Lett.*, 2005, **94**, 045504.
- 33 A. J. Bridgeman and G. Cavigliasso, *Inorg. Chem.*, 2002, **41**, 1761.
- 34 L. Yan, X. Lopez, J. J. Carbo, R. Sniatynsky, D. C. Duncan and J. M. Poblet, *J. Am. Chem. Soc.*, 2008, **130**, 8223.
- 35 A. J. Bridgeman and G. Cavigliasso, *Chem. Phys.*, 2002, **279**, 143.
- 36 K. H. Tytko, J. Mehmke and S. Fischer, *Struct. Bonding*, 1999, **93**, 129.
- 37 W. Kabsch, *Acta Crystallogr.*, 1976, **32**, 922.
- 38 N. Kuganathan and J. C. Green, *Int. J. Quantum Chem.*, 2008, **108**, 797.
- 39 T. W. Chamberlain, J. C. Meyer, J. Biskupek, J. Leschner, A. Santana, N. A. Besley, E. Bichoutskaia, U. Kaiser and A. N. Khlobystov, *Nat. Chem.*, 2011, **3**, 732.
- 40 A. Skoulidas, D. M. Ackerman, D. S. Scholl and J. K. Johnson, *Phys. Rev. Lett.*, 2002, **89**, 185901.
- 41 J. K. Holt, H. G. Park, Y. Wang, M. Stadermann, A. B. Artyukhin, C. P. Grigoropoulos, A. Noy and O. Bakajin, *Science*, 2006, **312**, 1034.
- 42 A. Gómez-Rodríguez, L. M. Beltrán Del Río and R. Herrera-Becerra, *Ultramicroscopy*, 2010, **110**, 95.
- 43 S. J. Clark, M. D. Segall, C. J. Pickard, P. J. Hasnip, M. J. Probert, K. Refson and M. C. Payne, *Z. Kristallogr.*, 2005, **220**, 567.